Surface modification of highly oriented pyrolytic graphite by reaction with atomic nitrogen at high temperatures

Luning Zhang [a,1], Dušan A. Pejaković [a,*], Baisong Geng [b,2], Jochen Marschall [a]

[a] *Molecular Physics Laboratory, SRI International, 333 Ravenswood Avenue, Menlo Park, CA 94025, USA*
[b] *Department of Physics, University of California, Berkeley, CA 94720, USA*

ARTICLE INFO

ABSTRACT

Dry etching of {0 0 0 1} basal planes of highly oriented pyrolytic graphite (HOPG) using active nitridation by nitrogen atoms was investigated at low pressures and high temperatures. The etching process produces channels at grain boundaries and pits whose shapes depend on the reaction temperature. For temperatures below 600 °C, the majority of pits are nearly circular, with a small fraction of hexagonal pits with rounded edges. For temperatures above 600 °C, the pits are almost exclusively hexagonal with straight edges. The Raman spectra of samples etched at 1000 °C show the D mode near 1360 cm^{-1}, which is absent in pristine HOPG. For deep hexagonal pits that penetrate many graphene layers, neither the surface number density of pits nor the width of pit size distribution changes substantially with the nitridation time, suggesting that these pits are initiated at a fixed number of extended defects intersecting {0 0 0 1} planes. Shallow pits that penetrate 1–2 graphene layers have a wide size distribution, which suggests that these pits are initiated on pristine graphene surfaces from lattice vacancies continually formed by N atoms. A similar wide size distribution of shallow hexagonal pits is observed in an *n*-layer graphene sample after N-atom etching.

© 2011 Elsevier B.V. All rights reserved.

1. Introduction

Chemical reactions involving graphite have long played important roles in industrial processes, such as energy generation, steelmaking, and electrolysis. Different grades of graphite exhibit large property variations because of different impurity levels, grain sizes, grain boundaries, and amorphous inclusions, which complicate fundamental studies of these chemical reactions. Highly oriented pyrolytic graphite (HOPG) has attracted much attention because of its well-defined structure with exposed basal {0 0 0 1} surfaces and high level of parallelism of graphene layers in different grains. HOPG serves as an excellent platform for studying gas–solid surface reactions [1–5], self-assembly [6,7], metal–surface interaction [8], and templated growth of nanomaterials [9,10]. Investigations of HOPG surface reactions have recently gained in relevance as graphene has emerged as one of the most exciting novel materials due to its unique electronic properties [11]. Of particular interest are surface processes that produce anisotropic etching of graphene because they can be used to control the crystallographic orientation of graphene edges. This orientation influences the graphene electrical and magnetic properties, and is thus crucial for the fabrication of graphene-based devices [11,12].

Studies of the surface modification of carbon by gas–solid reactions have had a long history. Oxidation experiments on HOPG specimens in air or O_2-containing gas mixtures have showed the generation of pits of various sizes and shapes on the basal plane depending on the reaction temperature, oxidant partial pressure, and defect concentrations [1,2,4,13–19]. For pristine HOPG surfaces, oxidation at temperatures up to around 700 °C seems to produce primarily shallow (1–4 graphene layers), quasi-circular etch pits, which appear to originate at localized intrinsic defects. It has been confirmed that the pit number density increases with defect density introduced by ion bombardment or inert gas plasma [13–16,20]. Deeper pits are also formed on oxidized HOPG and are thought to be associated with extended defects such as screw or edge dislocations along <0 0 0 1> directions (the *c*-axis) that transect many graphene layers [17,21]. Multilayer pits seem to grow several times faster than monolayer pits under the same oxidation conditions [16,17]. Monolayer pits appear to initiate at the same time and grow at similar rates, resulting in narrow size (diameter) distributions. However, at higher temperatures the size distribution of shallow pits becomes wider, indicating that the pits originate at different times by the reaction of O_2 with carbon atoms at perfect (non-defected) graphene locations as well as at defects [1,13].

---

* Corresponding author. Tel.: +1 650 859 5129; fax: +1 650 859 6196.
E-mail address: dusan.pejakovic@sri.com (D.A. Pejaković).
[1] Present address: Siemens Technology-To-Business Center, Shanghai, PR China.
[2] Visiting Ph.D. student. Permanent address: School of Physical Science and Technology, Lanzhou University, Lanzhou 730000, PR China.
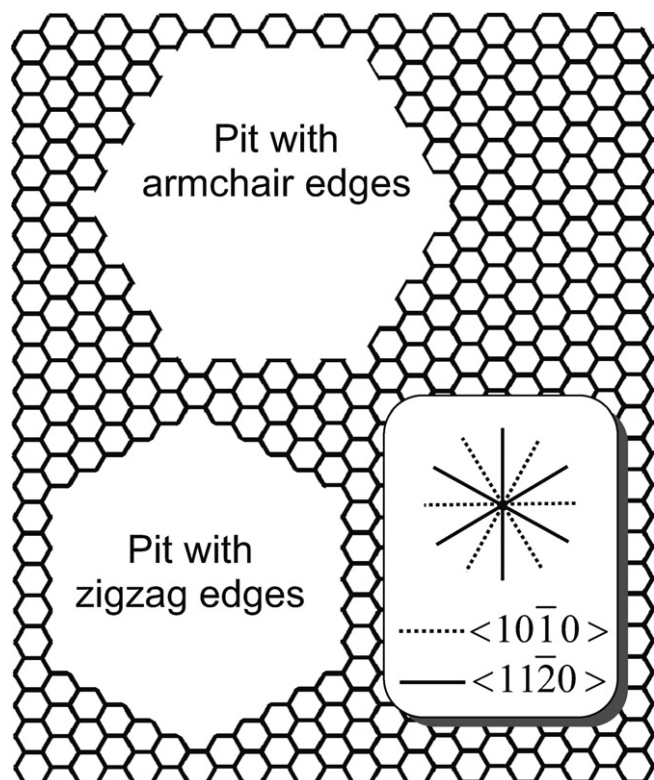
Fig. 1. Schematic of the {0 0 0 1} basal plane of graphite showing two possible orientations for hexagonal etch pits.

In addition to the predominant circular etch pits, some hexagonal pits have also been observed in HOPG oxidized in O_2 [1,2,18]. The hexagonal shape indicates that etching is anisotropic, i.e., that carbon removal by O_2 is more efficient along a particular family of crystallographic directions in the basal plane: the $< 10\bar{1}0 >$ or $< 11\bar{2}0 >$ directions. Fig. 1 illustrates the two possible orientations of perfect hexagonal pits in a graphene sheet. A graphene sheet cut parallel to a $< 10\bar{1}0 >$ direction at the atomic level forms an "armchair" edge and one cut parallel to a $< 11\bar{2}0 >$ direction forms a "zigzag" edge. Optical microscopic measurements performed in the 1960s on natural Ticonderoga graphite single crystals oxidized at 700–900 °C showed that large hexagonal etch pits grow with their edges parallel to twin bands aligned with $< 10\bar{1}0 >$ directions, implying armchair edges [22,23]. The same hexagonal etch pit orientation was confirmed by Rodriguez-Reinoso and Thrower using electron diffraction on HOPG surfaces oxidized in the 700–750 °C range [24]. A study by Thomas et al. of oxidized Ticonderoga graphite crystals showed that the preferred crystallographic direction for etching by O_2 switches as temperature is increased; the hexagonal pits formed at 800 °C had edges in $< 10\bar{1}0 >$ directions, whereas the pits formed at 1000 °C had edges in $< 11\bar{2}0 >$ directions [25]. Hiura used scanning tunneling microscopy (STM) to show that that the edges of hexagonal pits on HOPG basal planes oxidized at a very high temperature (estimated near 2000 °C) during electron beam exposure are parallel to $< 11\bar{2}0 >$ directions [21].

Plasma treatments have been used to clean, roughen, or "activate" carbon surfaces for a variety of applications. Atomic oxygen generated by radio frequency or microwave discharge sources reacts more aggressively with carbon surfaces than molecular oxygen [26–28]. Early O-atom oxidation studies, by Marsh et al. [27] on a variety of carbon materials and by McCarroll and McKee [28] on Ticonderoga graphite, found relatively large hemispherical and conical etch pits. In the case of O-atom oxidation of HOPG basal planes (0.7 Torr pressure, temperatures up to 190 °C and exposure times up to 20 min), circular pits up to several micrometers in diameter and tens of nanometers in depth were formed, along with channels along grain boundaries [3,29]. The high density of etch pits and wide distribution of pit sizes resulting from O-atom oxidation suggests that even at temperatures below 200 °C atomic oxygen can abstract carbon atoms directly from a pristine graphene sheet. Oxidation by O_2, on the other hand, initiates etch pits only at intrinsic defects even at temperatures up to ∼700 °C. Wong et al. performed O-atom oxidation of single-crystal Ticonderoga graphite (1 Torr, 150 °C, 5 min) and found some hexagonal pits with edges parallel to $< 11\bar{2}0 >$ directions [30].

While the rate of carbon nitridation by N_2 is insignificant compared to that of carbon oxidation by O_2, interesting and important chemical interactions between carbon surfaces and reactive nitrogen species are known. Some examples include the formation of hard carbon nitride films by plasma nitridation [31], the n-doping of graphene by reaction with nitrogen-bearing species [32], and the formation of gaseous CN by the high-temperature reaction of graphite with atomic nitrogen [33,34]. The latter, "active" nitridation reaction is important for predicting the performance of carbon-based ablative thermal protection systems for high-speed atmospheric reentry vehicles [35]. We have recently determined that approximately three carbon atoms are removed per 1000 N-atom collisions with the surface of isotropic polycrystalline graphite at 1000 °C and N-atom concentrations on the order of 1×10^{-4} mol m^{-3} [34]. The earliest studies of single-crystal graphite surfaces exposed to atomic nitrogen are those of McCarroll and McKee [28,36]. They exposed flakes of Ticonderoga graphite to microwave-dissociated nitrogen at a total pressure of 2 Torr and temperatures up to 1139 °C in a fast-flow reactor, and used optical and scanning electron microscopy to characterize the resulting morphology [28,36]. They found shallow, hemispherical pits at 720 °C and well-defined hexagonal pits at 1100 °C and 1138 °C. The hexagonal pits had edges parallel to $< 10\bar{1}0 >$ directions, implying armchair edges. More recently, O'Kell et al. [37] used a low-power radio-frequency discharge to expose graphite and HOPG surfaces to nitrogen plasma and demonstrated roughening of the surface but did not observe any hexagonal etch pits. In the latter study, samples were placed directly in the plasma at an unspecified temperature.

While published studies mentioned above [28,36] suggest that anisotropic dry etching by N atoms in graphite basal plane is possible, much is still unknown about this process and the optimal reaction conditions for producing such surface etching have not been determined. In the few studies published to date the reaction parameters have not been characterized well. One significant issue with plasma exposure studies is that the reactive environment is seldom well-defined. If specimens are placed directly in the discharge region, they are exposed to a mixture of electrons, ions, atoms and molecules in various excited states, and a variety of competing surface reaction mechanisms may operate in parallel. In previous studies, the concentrations of these reactive species at the sample location were difficult to determine and were not reported. Experiments with specimens placed sufficiently downstream of the discharge region, such as the experiments reported here, have the advantage that populations of charged and excited species are insignificant, so that surface reactions can be attributed to one dominant reactive species, in this case N atoms.

Here, results are presented on the surface morphologies of HOPG and n-layer graphene samples that result from etching by N-atom nitridation. The reaction conditions in this study have been defined much better than in previous studies. Nitridation is performed in a flow reactor coupled to a microwave discharge and a tube furnace. The N-atom concentration at the sample location is constrained by measurements of N-atom concentrations entering and exiting the furnace using a gas-phase titration technique. Atomic

force microscopy (AFM), scanning electron microscopy (SEM), and Raman spectroscopy are used to characterize the modifications of the HOPG basal plane by etching. Limited experiments are also conducted on *n*-layer graphene. It is confirmed that efficient anisotropic etching of HOPG and *n*-layer graphene can be achieved by N-atom active nitridation. The morphology and size distribution of etch pits produced at different temperatures are discussed in detail.

2. Experimental

2.1. Materials

The HOPG specimens were acquired from SPI Supplies (SPI-2 grade). This grade of HOPG has a specified grain size of 0.5–1 μm and a mosaic angle of 0.8° ± 0.2°. The mosaic angle is a measure of parallelism of graphene layers in different grains, with smaller values reflecting greater uniformity. Before each experiment, HOPG specimens were cut into 5 mm × 5 mm or 2 mm × 5 mm pieces and then cleaved using either adhesive tape or a razor blade. The final sample thickness was about 0.5 mm. To investigate whether nitridation by N atoms of another form of highly oriented graphite exhibits similar behavior, we also performed a limited number of experiments with *n*-layer graphene samples (7–10 layers) made from Kish graphite (Covalent Materials, AP70 grade). These samples were prepared by mechanically exfoliating the basal plane of a Kish graphite specimen using adhesive tape and then pressing the exfoliated flakes against a SiO$_2$/Si wafer (300 nm oxide layer).

2.2. Nitridation of materials

The nitridation setup consisted of a 100 W microwave discharge unit coupled to a quartz flow tube inserted through a high-temperature tube furnace. A quartz boat holding a specimen was loaded into the flow tube near the center of the furnace prior to heating. The distance between the discharge cavity and specimen was about 78 cm. Nitrogen was introduced upstream of the discharge through an electronic mass flow controller and evacuated downstream of the furnace by a dry scroll pump. During heating and cooling, pure N$_2$ flow was used. Upon reaching the desired temperature, the discharge was turned on to start the N-atom nitridation process, or a particular gas mixture was introduced to study the effects of gas composition. Experiments were performed at furnace temperatures from 500 to 1000 °C, in 100 °C increments. In some experiments, oxygen was added to the molecular nitrogen flow at the titration port upstream of the furnace. Nitrogen (Ultra High Purity, 99.999%), oxygen (Research Purity, 99.9999%), and nitric oxide (Ultra High Purity, 99.5%) gases were obtained from Matheson Tri-Gas and used as-received.

Activation of the discharge dissociated a fraction of the molecular nitrogen flow. The N-atom concentration at the sample location was determined as follows. The total gas pressures were mea-
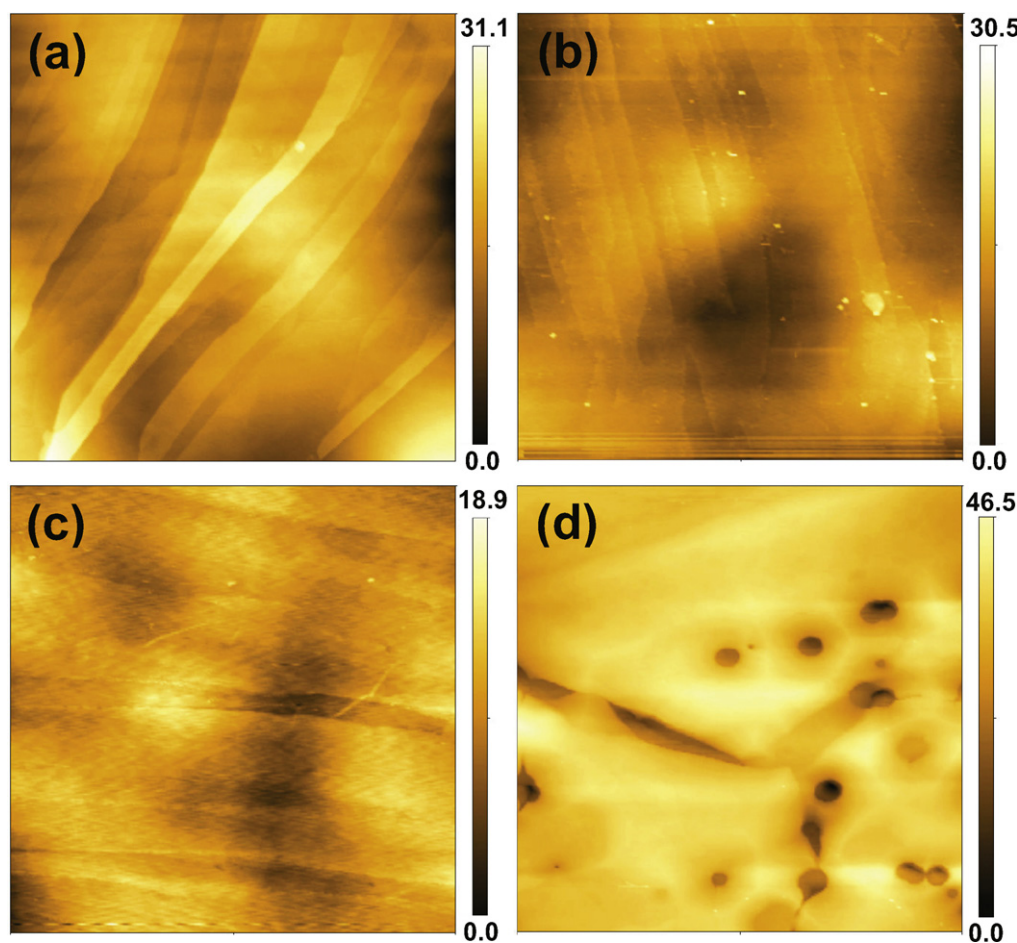

Fig. 2. Comparison of HOPG sample surfaces after different treatments: (a) pristine surface after cleavage; (b) pure N$_2$ flow at 1000 °C for 310 min; (c) O$_2$/N$_2$ flow at 600 °C for 130 min ($C_{O_2} = 6.8 \times 10^{-5}$ mol m^{-3}, $P = 1.87$ Torr). (d) N/N$_2$ flow at 500 °C for 80 min ($C_N = 5.9 \times 10^{-5}$ mol m^{-3}, $P = 1.88$ Torr). All AFM images are 5.13 μm × 5.13 μm in size.
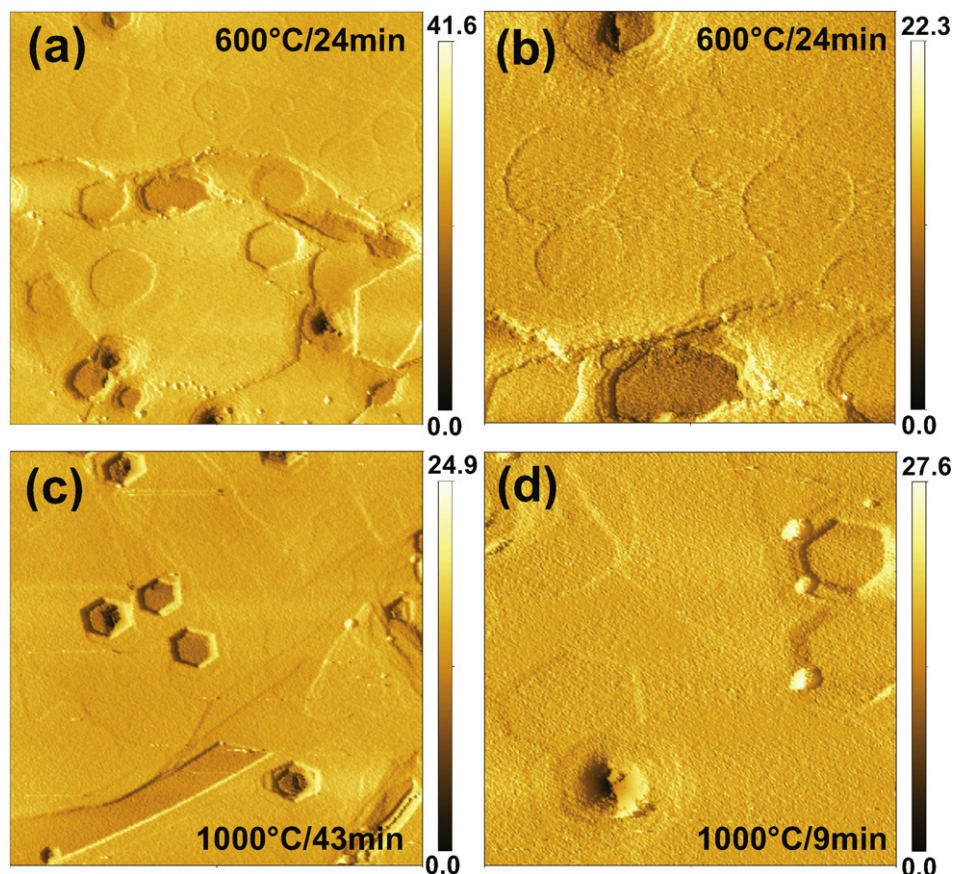
Fig. 3. Comparison of HOPG surfaces after nitridation at 600 °C and 1000 °C as imaged by AFM. Shallow and deep circular pits are shown in (a). A close-up of the upper region of (a) is shown in (b). Several deep hexagonal pits near channels are shown in (c). Shallow and deep hexagonal pits of different depths are shown in (d). Image sizes are 1.46 μm × 1.46 μm for (a) and (c); and 0.73 μm × 0.73 μm for (b) and (d).

sured upstream and downstream of the furnace using capacitance manometers. The gas temperature at these locations was assumed equal to the surface temperature of the flow tube wall, measured using type K thermocouples. The mole fractions of atomic nitrogen entering and exiting the furnace were measured by gas-phase titration with nitric oxide that was added incrementally through a flow controller. The titration reaction $N + NO \rightarrow N_2 + O$ is rapid, with a room-temperature rate coefficient of 3×10^{-11} cm^3 mol^{-1} s^{-1} [38]. At the titration endpoint all the N atoms are consumed in the reaction and their number density is equal to the number density of added NO molecules, which is calculated from the measured NO flow rate. The fast titration reaction ensures that all N atoms in the flow are consumed rapidly within a short distance from the titration ports. The endpoint was determined using a residual gas analyzer (Stanford Research Systems, RGA200) to detect the excess NO that appears once the endpoint has been passed.

Because the total gas pressure and the N-atom mole fraction at the sample location must lie between their upstream and downstream values, the above set of measurements, together with the furnace temperature, provides enough information to set the upper and lower limits of the N-atom concentration at the sample location. For example, for the tests conducted at 1000 °C, the upstream and downstream N-atom mole fractions are 0.38% and 0.19%, respectively, and the mole fraction at the sample location must lie between these values. Tighter constraints for the N-atom concentration at the sample location were obtained by interpolation, using a one-dimensional reactive-flow model that incorporates the Hagen-Poisseulli flow relation, the ideal gas law, and N-atom losses by gas-phase and surface recombination. Details of this model and

experimental approach are presented elsewhere [34]. Using this procedure, we have obtained the following test conditions at the sample location for data presented in this paper. For tests done at 500 °C, the N-atom concentration was 5.9×10^{-5} mol m^{-3} at a total pressure of 1.88 Torr. For 600 °C, the N-atom concentration was 3.7×10^{-5} mol m^{-3} at a pressure of 1.87 Torr. For 1000 °C, the N-atom concentration was 5.8×10^{-5} mol m^{-3} at a pressure of 1.83 Torr. The estimated 1-σ uncertainty of the measured N-atom concentration is 10%. The bulk flow velocity at the sample location was maintained at about 28.0 m s^{-1} for all temperatures by adjusting the N_2 flow rate.

2.3. Characterization methods

AFM imaging was performed on a Pacific Nanotechnology Nano-R instrument. SEM images were obtained with a JEOL 6100 field-emission scanning electron microscope. Raman spectroscopy was performed using a home-built micro-Raman apparatus. The excitation source was a diode laser operating at a wavelength of 532 nm with an output power less than 5 mW. The laser beam was focused to a spot size of about 1 μm on the sample surface. The Stokes Raman signal was collected through a 40× objective with a numerical aperture of 0.6 and dispersed by a spectrograph onto a liquid nitrogen-cooled CCD detector. For each sample, several spectra were collected at different positions along a scan line, about 10 μm long. There was no significant variation of the spectra along the scanned linear region.

3. Results and discussion

3.1. Effects of reactant gas

In Fig. 2, AFM images of samples treated in different atmospheres are shown in order to understand the effects of gas composition and possible O_2 impurities. Fig. 2a shows the topography of a pristine HOPG surface. Fig. 2b shows the surface of a sample treated in pure N_2 flow at 1000 °C for 310 min and Fig. 2c shows the surface of a sample after 130 min in an O_2/N_2 mixture (molar ratio 0.3/100) at 600 °C. No obvious changes in topography are found after these two surface treatments. Several particles are observed in Fig. 2b, possibly due to adhesive residue from sample preparation by tape-cleavage [39]. Fig. 2d shows the surface of a sample exposed to an N/N_2 mixture (molar ratio 0.2/100) at 500 °C for 80 min. Significant modification to the surface in the form of pits and channels produced by nitrogen atoms is evident.

Although O_2 can react with HOPG in the 500–600 °C temperature range, we found that N atoms are substantially more reactive than O_2 at similar molar concentrations, causing obvious topographic changes to the HOPG basal plane (Fig. 2c and d). This implies that surface modification due to oxidation by oxygen impurities or residual air leaks in the system is insignificant. These results also confirm that active nitridation of HOPG by N_2 is negligible under our experimental conditions.

3.2. Effects of temperature on the shape of pits

Fig. 3a and b shows the HOPG surface after N-atom nitridation at 600 °C for 24 min, and Fig. 3c and d shows surfaces after nitridation
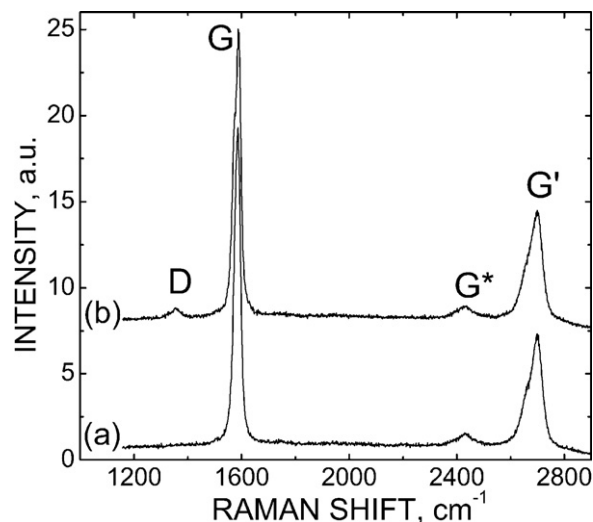

Fig. 4. Raman spectra of HOPG: (a) pristine surface after cleavage; (b) surface after 21 min of nitridation at 1000 °C. Each spectrum is an average of multiple spectra at several positions.

at 1000 °C for 43 and 9 min, respectively. Although the figures show pits with various shapes and depths, we can categorize them in two groups: shallow pits (less than 1 nm deep) and deep pits (from several nanometers to tens of nanometers deep). These two types of pits appear after nitridation at all temperatures from 600 °C to 1000 °C.
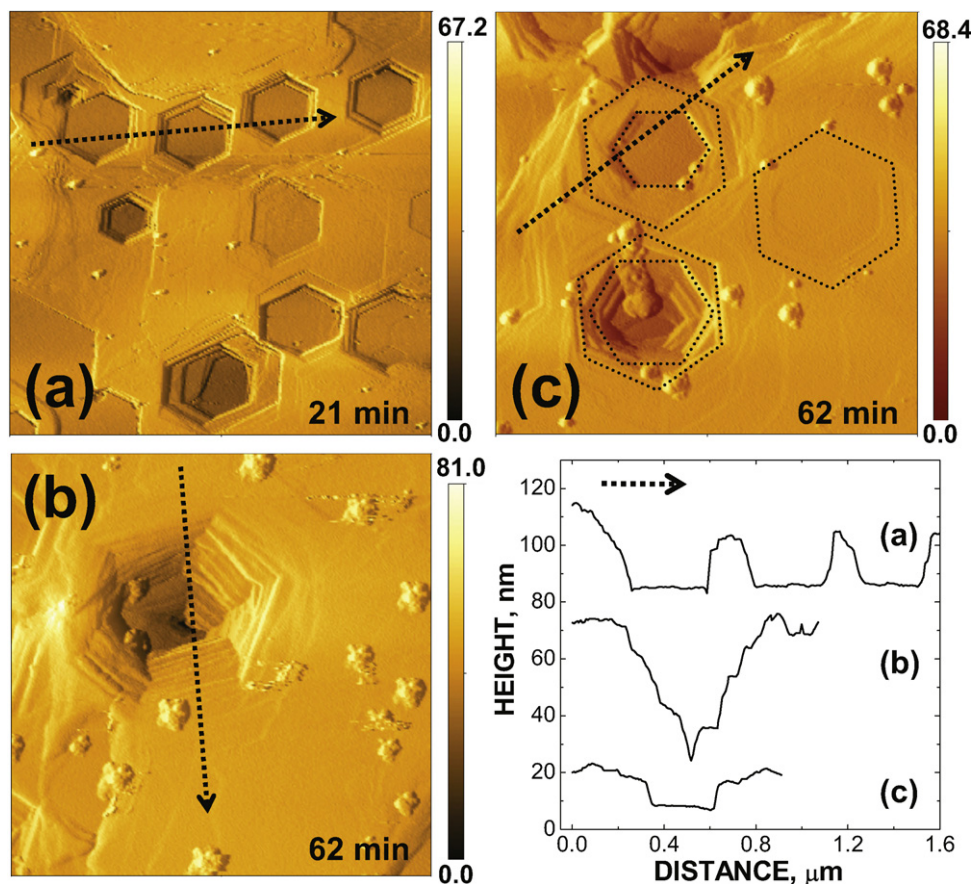

Fig. 5. Different HOPG surface morphologies revealed by AFM after nitridation at 1000 °C: (a) typical deep hexagonal pits; (b) a deep terraced pit; (c) terraced hexagonal pits showing a 30° rotation. Reaction time is shown in each figure. Depth profiles of the line scans, indicated by arrows in (a), (b), and (c), are shown in the bottom right panel. Image sizes: (a) 2.2 μm × 2.2 μm; (b) and (c) 1.46 μm × 1.46 μm.

Most shallow pits are either ∼0.35 nm or ∼0.7 nm in depth. Given that the separation between adjacent graphene layers in graphite is 0.335 nm, these depths correspond to 1 or 2 etched graphene layers. The shallow pits imaged in Fig. 3a and b have a variety of diameters (ranging from ∼20 nm to ∼100 nm), indicating that they were formed at different times during the nitridation process. This suggests that N atoms are able to initiate shallow pits not only at preexisting defects, but also on a pristine graphite surface without defects. One interesting finding is that it is more difficult to find shallow pits on samples after 1000 °C nitridation. In Fig. 3d, several shallow pits are shown after 9 min of nitridation. For longer nitridation times, we only observed sub-nanometer steps and extended shallow features together with deep hexagonal pits and channels. This is evident in the upper region in Fig. 3c. It is obvious that lateral removal of carbon atoms by N atoms is fast at 1000 °C, leading to the removal of large areas of graphene layers. Hence, any formed shallow pits seem to expand rapidly during nitridation at 1000 °C, resulting in large shallow features without well-defined hexagonal boundaries.

An important observation in Fig. 3 is that the shape of etch pits changes with the reaction temperature. At 500 °C (Fig. 2d) and 600 °C (Fig. 3a and b), the pits are mostly circular, with some semi-hexagonal pits with rounded edges and corners. Circular pits imply that carbon removal by N atoms does not have a strong directional preference within the basal plane. At temperatures above 600 °C, the pits are almost exclusively hexagonal with straight edges. The well-defined hexagonal pits indicate that net carbon removal is significantly more efficient along one of the crystallographic directions. No significant changes in the general morphology of etch pits was observed between 700 °C and 1000 °C, therefore in this paper we do not show images of samples treated at intermediate temperatures.

On the atomic scale, the geometric evolution of the etch pit edges likely involves multiple bond-breaking, bond-forming, and bond-reconstruction events as revealed recently by TEM studies [40,41]. However, on a mesoscopic scale, the temperature dependence of the pit shapes can be understood using a simple activation energy argument. The transition from circular to hexagonal pit shapes with increasing temperature suggests that the cumulative effect of the nitridation reaction can be described by effective activation energies for carbon removal that differ along the two principal directions. In the simplest case, we can assume that the nitridation reaction rates follow an Arrhenius behavior with temperature-independent activation energies and pre-exponential
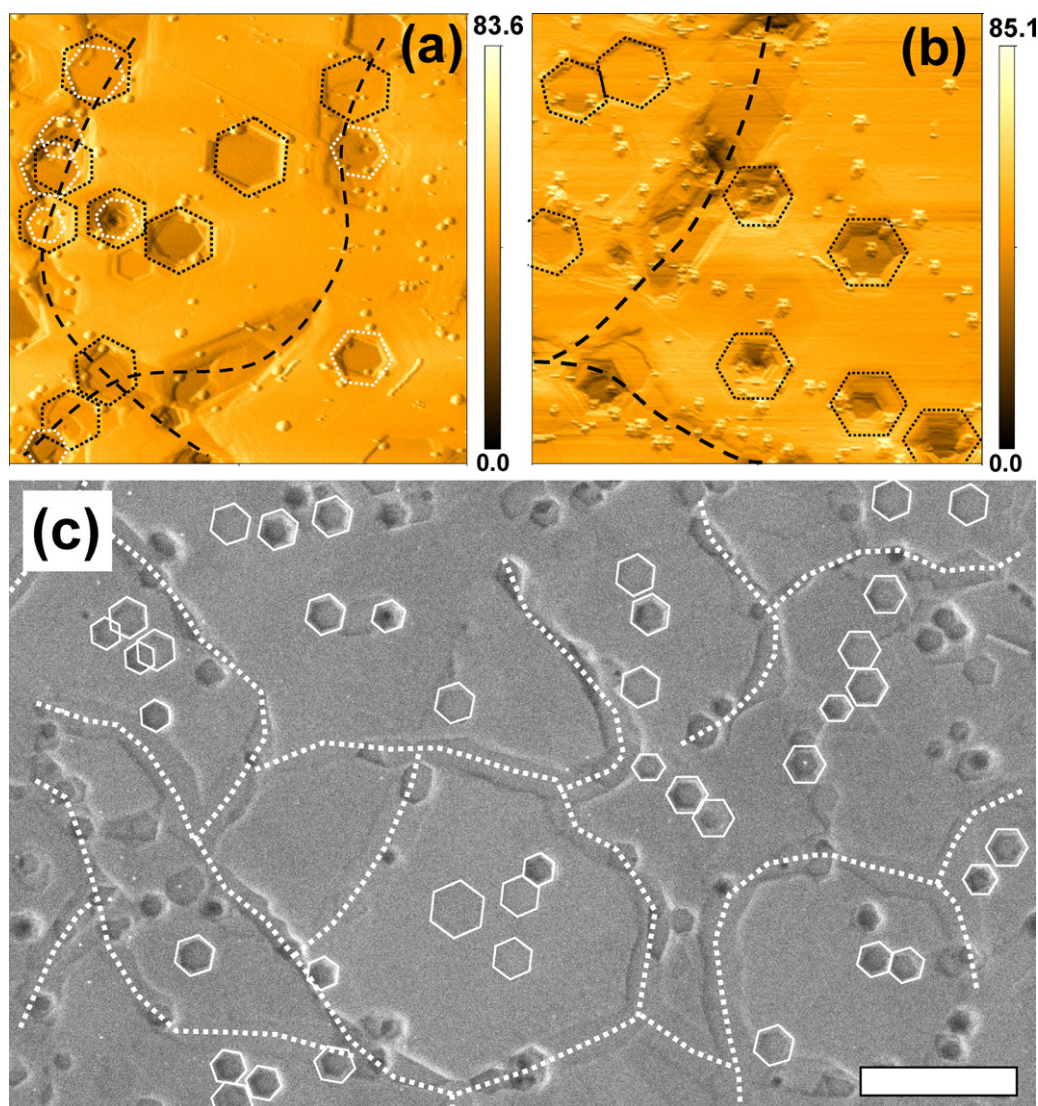

Fig. 6. Images of HOPG surface after nitridation at 1000 °C: (a) AFM image showing arrays of overlapping hexagonal pits within channels; (b) AFM image showing different pit orientations on two sides of a channel; (c) SEM image showing channels and hexagonal pits with hexagons and dotted lines overlaid on these features. The reaction time for (a) and (b) is 62 min and the image size is 3.66 μm × 3.66 μm. The reaction time for (c) is 21 min and the scale bar is 2 μm.
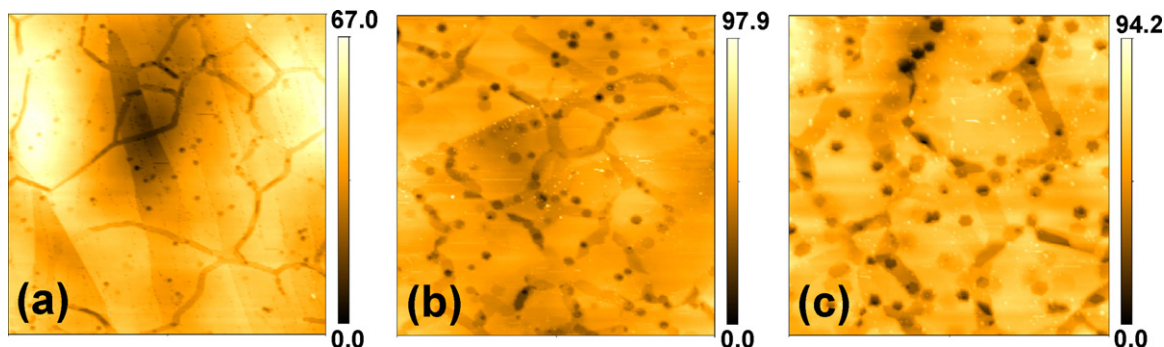
Fig. 7. Formation of pits and channels on three HOPG samples after nitridation at 1000 °C for (a) 9 min, (b) 24 min, and (c) 62 min. The gas pressure and N-atom concentration are provided in the experimental section. All images are 10.25 μm × 10.25 μm in size.

factors. Hence, the experimental results can be interpreted as follows. At low temperatures, the reaction rates along $<10\bar{1}0>$ and $<11\bar{2}0>$ directions are similar although they have different activation energies; the difference in activation energies is compensated by different pre-exponential factors. With increasing temperature the nitridation reaction along the direction with lower activation energy begins to dominate and pit shapes become increasingly hexagonal.

Fig. 4 compares the Raman spectrum of a pristine HOPG surface with a spectrum from a sample etched for 21 min at 1000 °C. As shown in trace (a), a freshly cleaved HOPG surface shows three Raman features in the 1000–3000 cm^{-1} range: the G mode at ∼1585 cm^{-1}, the G* mode at ∼2430 cm^{-1}, and the G′ mode at ∼2700 cm^{-1}. The G mode arises from the in-plane vibration of C–C bonds with E_{2g} symmetry. The G* and G′ modes are due to double resonance scattering processes involving two phonons: two in-plane transverse optical phonons (G*) or the combination of a longitudinal phonon and a transverse phonon (G′) [42,43]. An additional Raman feature appears at ∼1360 cm^{-1} for the etched sample, as shown in trace (b) in Fig. 4. This feature is the D mode which originates from a defect-induced Raman process consisting of four steps: (1) photo-excitation of an electron–hole pair, (2) inelastic scattering of the electron (or hole) by a phonon, (3) elastic scattering of the electron (or hole) by a defect, and (4) recombination of the excited electron and hole [44,45].

In our data, the contribution to the D band by step-edges can be ruled out by comparing traces (a) and (b) in Fig. 4. Since the Raman spectra were obtained by several linear scans along a 10 μm distance, and step-edges appear both on the pristine and nitridated HOPG surfaces, D band should be observed for the pristine sample if step-edge contribution is large. Thus, the appearance of the D band is due to features produced by N-atom etching, i.e., channels and hexagonal pits. The Raman process in graphite and *n*-layer graphene has been studied extensively, and it has been shown both theoretically and experimentally that the D band is strong at armchair edges, but very weak at zigzag edges [44–46]. The presence of the D band in our data would thus suggest an increased population of armchair edges on the etched surface, implying that hexagonal pits grow preferentially by removing carbon atoms along the $<11\bar{2}0>$ directions. However, given that the D band is not absent at zigzag edges, we cannot claim this with certainty before an atomic-resolution study, such as STM, is performed. We note, however, that the formation of armchair edges would be consistent with the observation of McCarroll and McKee, who concluded that armchair edges were formed by N-atom nitridation of Ticonderoga graphite at ∼1100 °C [28,36].

In the following two sections, we will focus on nitridation experiments at 1000 °C, which produce nearly perfectly shaped deep hexagonal pits and networks of deep channels.

3.3. Morphology of multilayer pits and channels at 1000 °C

Typical surface morphology of a sample etched at 1000 °C is shown in Fig. 5a. In addition to shallow pits with depths of 1–2 graphene layers, significantly deeper hexagonal pits and channels are formed. Some hexagonal pits are also observed within channels. Most deep hexagonal pits have flat bottoms, relatively vertical edges and large width-to-depth ratios. This morphology is consistent with the following notions: deep pits form at extended defects propagating along the *c*-axis, pit depth is determined by the vertical
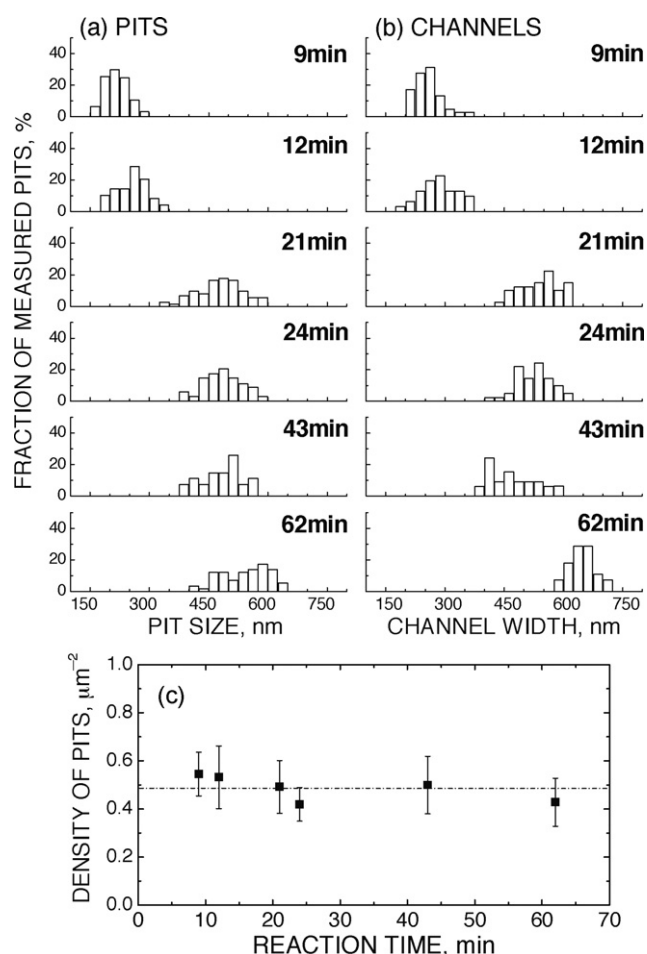

Fig. 8. Plots of the (a) size of the hexagonal pits, (b) channel width, and (c) pit number density versus nitridation time at 1000 °C. The horizontal line in (c) represents the mean pit density calculated from all samples. The nitridation conditions are provided in Section 2.
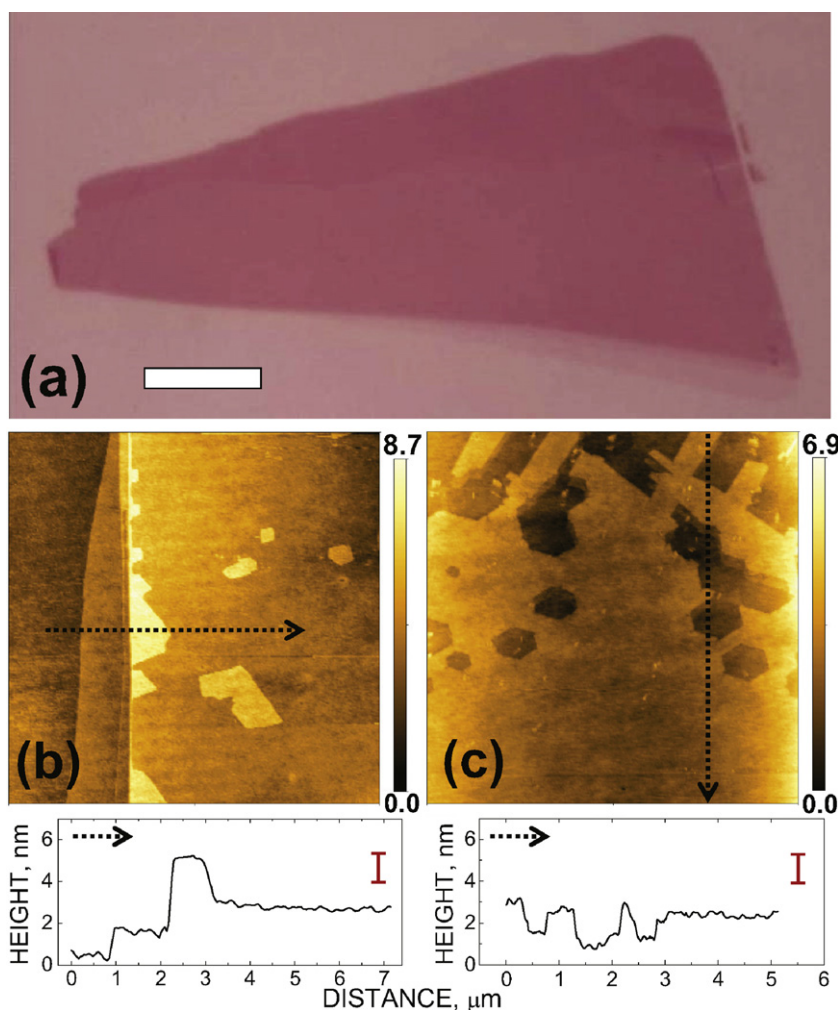
Fig. 9. Results for an *n*-layer graphene sample (*n* = 7–10) on a SiO$_2$/Si substrate: (a) optical image before nitridation (scale bar is 10 μm); (b) AFM image before nitridation; (c) AFM image after nitridation at 1000 °C for 14 min. Height profiles of the line scans in (b) and (c) are shown under each image. Scale bar in height profile corresponds to 4 graphene layers. Image sizes: (b) 10.25 μm × 10.25 μm; (c) 5.13 μm × 5.13 μm.

extent of the defects, and lateral etching of all transected graphene layers occurs at similar rates.

Deep terraced pits are also observed, although they occur less frequently. Fig. 5b shows a deep etch pit, which extends downward from the surface to a depth of about 50 nm in a series of concentric hexagonal terraces. Each terrace is comprised of multiple graphene sheets that have been etched laterally at the same rate, similar to the pits shown in Fig. 5a. Fig. 5c shows terraced hexagonal pits in which the deeper terraces are rotated about the *c*-axis with respect to the top hexagon. The large dashed hexagons in Fig. 5c outline the orientation of the topmost terraces of three etch pits; in this particular case, the top terrace is about 3.5 nm thick, as measured by an AFM line scan. The two smaller dashed hexagons in Fig. 5c outline deeper terraces, which appear to be rotated by about 30°. It seems unlikely that the favored crystallographic direction for etching in the basal plane would change with depth. Rather, these images suggest that the local HOPG structure contains a stacking defect that rotates the crystallographic orientation of adjacent graphene sheets by 30°, switching the $< 10\bar{1}0 >$ and $< 11\bar{2}0 >$ directions relative to the top layers.

The structural connection between hexagonal pits and channels can be seen in Fig. 6. Fig. 6a and b shows AFM images of regions separated by channels for a sample nitrided at 1000 °C for 62 min. Dashed lines are used to trace channels on the surface and dotted hexagons outline pits. Fig. 6a shows that arrays of hexagonal

pits are formed within channels; many of the pits overlap and have rotated terraces as in Fig. 5c. Fig. 6b shows that the orientation of hexagonal pits separated by a channel can differ significantly with respect to each other. An SEM image of a sample etched at 1000 °C for 21 min is shown in Fig. 6c, with channels marked by dotted lines and individual hexagonal pits highlighted by white hexagons. This SEM image shows a larger area than the AFM images in Fig. 6, and reinforces the conclusion that etched HOPG surface is comprised of channel-separated regions, within which groups of hexagonal pits all have the same orientation. The miss-orientation of hexagonal pits on different sides of a channel indicates that channels form along grain boundaries. Similar channels have been observed by AFM on HOPG after oxidation and were also assigned to grain boundaries [24,29]. The grain sizes determined from our AFM and SEM images are in the range 2–4 μm, larger than the specification of 0.5–1 μm provided by the HOPG supplier.

3.4. Time evolution of multilayer pits and channels at 1000 °C

The AFM images in Fig. 7 show the time evolution of pits and channels during nitridation at 1000 °C. Multi-layer hexagonal pits and channels are formed after only 9 min of reaction (Fig. 7a), and longer reaction times result in larger pits and wider channels (Fig. 7b and c). The size distribution of multi-layer pits and channels at different reaction times is plotted in Fig. 8a and b. Here we

define a multi-layer pit as at least 2 nm deep and size as the distance between the parallel edges of a channel or a hexagonal pit. The mean width of the channel is typically ~20% greater than that of the hexagonal pits at a given nitridation time. The size distributions shift to larger mean sizes with increasing exposure time but distribution widths remain relatively unchanged at about 200 nm. The general trend of increasing pit and channel width with reaction time is obvious. Previous oxidation studies on HOPG by O_2 molecules found that the sizes of monolayer and multilayer pits grow linearly with time [16,17]. From our nitridation results, we cannot conclude that the growth of deep hexagonal pits is linear as a function of time.

From Fig. 7a–c, the number of multilayer pits does not seem to change significantly during nitridation. The pit number densities were quantified as a function of reaction time in Fig. 8c. The pit density is nearly time-independent and, along with the relatively constant width of the pit size distribution, supports the notion that these multilayer pits initiate at pre-existing extended defects at about the same time and grow in size at similar rates. This behavior contrasts that observed for shallow pits, which seem to be initiated on defect-free HOPG surface as well as at defects, as discussed above.

3.5. Nitridation of n-layer graphene

Fig. 9a is an optical image of an *n*-layer graphene flake on a SiO_2/Si wafer. The main portion of the flake is 7–10 graphene layers thick. The image barely resolves a thinner region that is 1–2 graphene layers thick at the bottom edge of the sample. This thin region was resolved by AFM, as shown in Fig. 9b and the accompanying height profile of the AFM line scan. Some small graphene patches appear on top of a larger uniform graphene sheet in the as-prepared sample. These patches usually have thickness of 4–5 graphene layers.

Fig. 9c shows an AFM image of the *n*-layer graphene flake surface after nitridation at 1000 °C for 14 min under the same conditions as those used for the HOPG samples in Fig. 6. Hexagonal pits were formed with a wide range of sizes from about 150 to 700 nm, but all with depths equivalent to either 3 or 4 graphene layers. This can be seen from the height profile of the line scan in Fig. 9c. The formation of hexagonal pits on *n*-layer graphene confirms that N atoms react with C atoms in the basal plane preferentially along a specific crystallographic axis under these test conditions, as in the case of HOPG. All pits have the same orientation, indicating that the imaged part of the *n*-layer graphene sample presents a single grain. The wide pit size distribution suggests stochastic pit initiation on the *n*-layer graphene surface during nitridation, similar to the mechanism for shallow pit formation on HOPG surfaces at locations without defects, discussed above.

4. Conclusions

It was found that active nitridation of HOPG in N/N_2 mixtures readily produces pits and channels at temperatures from 500 to 1000 °C. Temperature has a pronounced effect on the shape of the pits. At 600 °C or below, circular and rounded–hexagonal pits are formed preferentially, indicating similar reaction probabilities along $< 11\bar{2}0 >$ and $< 10\bar{1}0 >$ directions. At temperatures above 600 °C, pits shaped as well-defined hexagons are formed, indicating anisotropic etching by N atoms. Analysis of the pit surface density and size distribution suggests that formation of deep hexagonal pits is initiated at a fixed number of extended defects intersecting the basal plane. The nitridation reaction also occurs preferentially at grain boundaries, most probably because of the higher density of extended defects there, forming channels that are similar in width

to deep hexagonal pits. Our results suggest that shallow pits (1–2 graphene layers thick) are initiated in a stochastic manner on HOPG surface regions free of extended defects. Similar experiments on *n*-layer graphene (*n* = 7–10) also produce shallow hexagonal pits at 1000 °C, with a depth equal to 3 and 4 graphene layers. The results for *n*-layer graphene agree with our proposed mechanism for shallow pits formation in HOPG.

Anisotropic etching of graphene, demonstrated here for N-atom nitridation, can be used to modify and fabricate templates and devices made of single-layer and *n*-layer graphene sheets with defined edge structures [11]. The appearance of the Raman D mode in etched samples supports the earlier reports of the formation of armchair edges upon N-atom nitridation of graphite at a similar temperature [28,36], although an atomic-resolution imaging study is needed to confirm this conclusion. In contrast, anisotropic etching of graphene by other methods, notably hydrogen plasma [12], has been shown to produce edges with zigzag orientation. Thus, dry etching by different reactive species can potentially be used for easy control of edge orientation in the production of graphene-based devices. Fabrication of HOPG surfaces with deep hexagonal pits may also prove useful for pit-templated synthesis [8,9,47] and micropatterned cell adhesion [48].

References

[1] H. Chang, A.J. Bard, J. Am. Chem. Soc. 113 (1991) 5588.
[2] X. Chu, L.D. Schmidt, Carbon 29 (1991) 1251.
[3] J.I. Paredes, A. Martínez-Alonso, J.M.D. Tascón, Carbon 38 (2000) 1183.
[4] A. Tracz, G. Wegner, J.P. Rabe, Langmuir 9 (1993) 3033.
[5] A. Tracz, G. Wegner, J.P. Rabe, Langmuir 19 (2003) 6807.
[6] F. Tao, S.L. Bernasek, Chem. Rev. 107 (2007) 1408.
[7] Y.H. Wei, K. Kannappan, G.W. Flynn, M.B. Zimmt, J. Am. Chem. Soc. 126 (2004) 5318.
[8] I. Lopez-Salido, D.C. Lim, Y.D. Kim, Surf. Sci. 588 (2005) 6.
[9] Y.-J. Zhu, A. Schneiders, J.D. Alexander, T.P. Beebe, Langmuir 18 (2002) 5728.
[10] M.P. Zach, K. Inazu, K.H. Ng, J.C. Hemminger, R.M. Penner, Chem. Mater. 14 (2002) 3206.
[11] A.K. Geim, K.S. Novoselov, Nat. Mater. 6 (2007) 183.
[12] R. Yang, L. Zhang, Y. Wang, Z. Shi, D. Shi, H. Gao, E. Wang, G. Zhang, Adv. Mater. 22 (2010) 4014.
[13] J.R. Hahn, Carbon 43 (2005) 1506.
[14] J.R. Hahn, H. Kang, J. Vac. Sci. Technol. A 17 (1999) 1606.
[15] J.R. Hahn, H. Kang, S.M. Lee, Y.H. Lee, J. Phys. Chem. B 103 (1999) 9944.
[16] S.M. Lee, Y.H. Lee, Y.G. Hwang, J.R. Hahn, H. Kang, Phys. Rev. Lett. 82 (1999) 217.
[17] F. Stevens, L.A. Kolodny, T.P. Beebe Jr., J. Phys. Chem. B 102 (1998) 10799.
[18] H. Chang, A.J. Bard, J. Am. Chem. Soc. 112 (1990) 4598.
[19] D. Tandon, E.J. Hippo, H. Marsh, E. Sebok, Carbon 35 (1997) 35.
[20] A. Tracz, A.A. Kalachev, G. Wegner, J.P. Rabe, Langmuir 11 (1995) 2840.
[21] H. Hiura, J. Mater. Res. 16 (2001) 1287.
[22] J.M. Thomas, E.E.G. Hughes, Carbon 1 (1964) 209.
[23] E.E.G. Hughes, J.M. Thomas, Nature 193 (1962) 838.
[24] F. Rodriguez-Reinoso, P.A. Thrower, Carbon 12 (1974) 269.
[25] J.M. Thomas, E.E.G. Huges, B.R. Williams, Philos. Mag. 8 (1963) 1513.
[26] A. Cuesta, A. Martínez-Alonso, J.M.D. Tascón, Carbon 39 (2001) 1135.
[27] H. Marsh, T.E. O'Hair, R. Reed, Trans. Faraday Soc. 61 (1965) 285.
[28] B. McCarroll, D.W. McKee, Carbon 9 (1971) 301.
[29] J.I. Paredes, A. Martínez-Alonso, J.M.D. Tascón, J. Mater. Chem. 10 (2000) 1585.
[30] C. Wong, R.T. Yang, B.L. Halpern, J. Chem. Phys. 78 (1983) 3325.
[31] B.B. Nayak, Surf. Coat. Technol. 201 (2006) 2639.
[32] X. Wang, X. Li, L. Zhang, Y. Yoon, P.K. Weber, H. Wang, J. Guo, H. Dai, Science 324 (2009) 768.
[33] C. Park, D.W. Bogdanoff, J. Thermophys. Heat Transfer 20 (2006) 487.
[34] L. Zhang, D.A. Pejaković, J. Marschall, D.G. Fletcher, AIAA Paper 2009-4251, 41st AIAA Thermophysics Conference, San Antonio, TX, 2009.
[35] Y.-K. Chen, F.S. Milos, J. Spacecraft Rockets 42 (2005) 961.

[36] B. McCarroll, D.W. McKee, Nature 225 (1970) 722.

[37] S. O'Kell, S. Pringle, C. Jones, J. Adhes. 56 (1996) 261.

[38] S.P. Sander, R.R. Friedl, D.M. Golden, M.J. Kurylo, G.K. Moortgat, H. Keller-Rudek, P.H. Wine, A.R. Ravishankara, C.E. Kolb, M.J. Molina, B.J. Finlayson-Pitts, R.E. Huie, V.L. Orkin, Chemical Kinetics and Photochemical Data for Use in Atmospheric Studies, Evaluation Number 15, JPL Publication 06-2, Jet Propulsion Laboratory, Pasadena, CA, 2006.

[39] L. Liu, S. Ryu, M.R. Tomasik, E. Stolyarova, N. Jung, M.S. Hybertsen, M.L. Steigerwald, L.E. Brus, G.W. Flynn, Nano Lett. 8 (2008) 1965.

[40] Ç.Ö. Girit, J. Meyer, R. Erni, M.D. Rossell, C. Kisielowski, L. Yang, C.-H. Park, M.F. Crommie, M.L. Cohen, S.G. Louie, A. Zettl, Science 323 (2009) 1705.

[41] X. Jia, M. Hofmann, V. Meunier, B.G. Sumpter, J. Campos-Delgado, J.M. Romo-Herrera, H. Son, Y.-P. Hsieh, A. Reina, J. Kong, M. Terrones, M.S. Dresselhaus, Science 323 (2009) 1701.

[42] J. Maultzsch, S. Reich, C. Thomsen, Phys. Rev. B 70 (2004) 155403.

[43] L.M. Malard, M.A. Pimenta, G. Dresselhaus, M.S. Dresselhaus, Phys. Rep. 473 (2009) 51.

[44] L.G. Cançado, M.A. Pimenta, B.R.A. Neves, M.S.S. Dantas, A. Jorio, Phys. Rev. Lett. 93 (2004) 247401.

[45] C. Casiraghi, A. Hartschuh, H. Qian, S. Piscanec, C. Georgi, A. Fasoli, K.S. Novoselov, D.M. Basko, A.C. Ferrari, Nano Lett. 9 (2009) 1433.

[46] Y. You, Z. Ni, T. Yu, Z. Shen, Appl. Phys. Lett. 93 (2008) 163112.

[47] Z. Song, T. Cai, J.C. Hanson, J.A. Rodriguez, J. Hrbek, J. Am. Chem. Soc. 126 (2004) 8576.

[48] N.D. Gallant, J.R. Capadona, A.B. Frazier, D.M. Collard, A.J. Garcia, Langmuir 18 (2002) 5579.